

Synergistic Heterointerface Coupling Enables Long-Life Sn-Based Anodes for Na-Ion Batteries

Yanqiong Li, Xiangfeng Fan, Ziyang Cai, Yingfei Li, and Huilin Pan*

Developing high-capacity and high-rate anodes for Na-ion batteries (NIBs) is important for practical use. Conventional hard carbon (HC) anodes exhibit good cycling performance, but the low specific capacity and potential Na plating pose significant challenges for their use in high-energy NIBs. Sn-based anodes, with appropriate Na storage potential and high capacity, hold great promise for high-performance NIBs. However, sluggish alloying kinetics and dramatic volume changes cause limited cycling life due to particle pulverization and repeated rupture of the solid electrolyte interphase (SEI). Here, a mechanical ball-milling process is used to construct a coupling heterointerface in the Sn/HC composite anode. The chemical–electrochemical coupling between

Sn and HC significantly lowers the alloying reaction barrier, enhances reversibility, and establishes additional rapid ion-transport pathways at the interface, thereby boosting reaction kinetics and stability. Simultaneously, local electrochemical-potential modulation effectively suppresses Sn volume expansion and stabilizes the SEI. As a result, the Sn/HC composite anode achieves over 12 000 cycles at current densities of 1.7 and 4.2 A g^{-1} . This study elucidates the role of constructing a rational chemical–electrochemical coupling heterointerface in addressing complex issues for alloy-based anode materials in high-energy applications.

1. Introduction

Na-ion batteries (NIBs) have attracted considerable attention for large-scale energy storage in recent years due to their low cost and relatively high energy density.^[1–3] Anode materials significantly influence the achievable energy density, power performance, and cycling life of NIBs.^[4,5] Hard carbon (HC) anodes possess a stable structure and good cycling performance among many kinds of anodes,^[6,7] but their theoretical capacity is limited ($\approx 300 \text{ mAh g}^{-1}$), and the potential Na plating at low potentials may cause safety issues and degrade the cycling life in practical use.^[8–10] Sn-based anodes, serving as an inexpensive and non-toxic alloy-type anode material, exhibit a low operating potential, high electrical conductivity, and a theoretical capacity of up to 847 mAh g^{-1} ,^[11] making them promising candidates for next-generation anodes for NIBs. However, similar to other alloy-type anodes, Sn suffers from sluggish alloying kinetics and experiences up to 420% volume expansion during cycling,^[12,13] leading to pulverization of active particles and repeated fracture of the solid electrolyte interphase (SEI), which in turn accelerates capacity decay.^[14–16]

To address the above challenges, a carbon-composite strategy that integrates the high capacity of Sn with conducting carbon-based material is regarded as one of the most effective approaches to extend the cycle life of Sn-based anodes.^[17–19] Many strategies have been proposed to provide a uniform carbon matrix for the Sn-based anode, for instance, Sn mixed with N-doped graphite nanosheets,^[20] encapsulated in carbon nanofibers,^[21] coated with porous carbon^[22] and embedded in the carbon network.^[23] However, most carbon-composite methods involve complex, costly processes and rely primarily on conductive networks or physical confinement to mitigate Sn aggregation and volume effects, which limits their effectiveness under high-rate and long-cycle conditions.^[24,25]

In this work, we use mechanical ball milling to fabricate a high-performance Sn/HC composite anode. By optimizing the mass ratio of Sn and HC, the chemical–electrochemical coupling reaction at the heterointerface between Sn and HC provides an additional reaction pathway in the Sn-based anodes. Appropriate heterointerface between Sn and HC substantially lowers the alloying energy barrier, while enhancing the reaction kinetics and reversibility of the Sn-based anode. As a result, the Sn/HC composite anode delivers an ultra-long cycling lifespan of 12 000 cycles at current densities of 1.7 A g^{-1} as well as 4.2 A g^{-1} . This study unveils an insightful strategy by using heterointerface design for cooperatively addressing the tangled issues in alloy-based anodes.

2. Results and Discussion

Figure 1a shows the synthesis procedure for constructing a heterointerface in Sn/HC composites via mechanical ball milling. Samples are denoted as Sn@HC-x-y, where x:y presents the mass

Y. Li, X. Fan, Z. Cai, Y. Li, H. Pan

Department of Chemistry

Zhejiang University

Hangzhou 310027, P. R. China

E-mail: panhuilin@zju.edu.cn

H. Pan

State Key Laboratory of Clean Energy Utilization

Zhejiang University

Hangzhou 310012, P. R. China

 Supporting information for this article is available on the WWW under <https://doi.org/10.1002/batt.202500412>

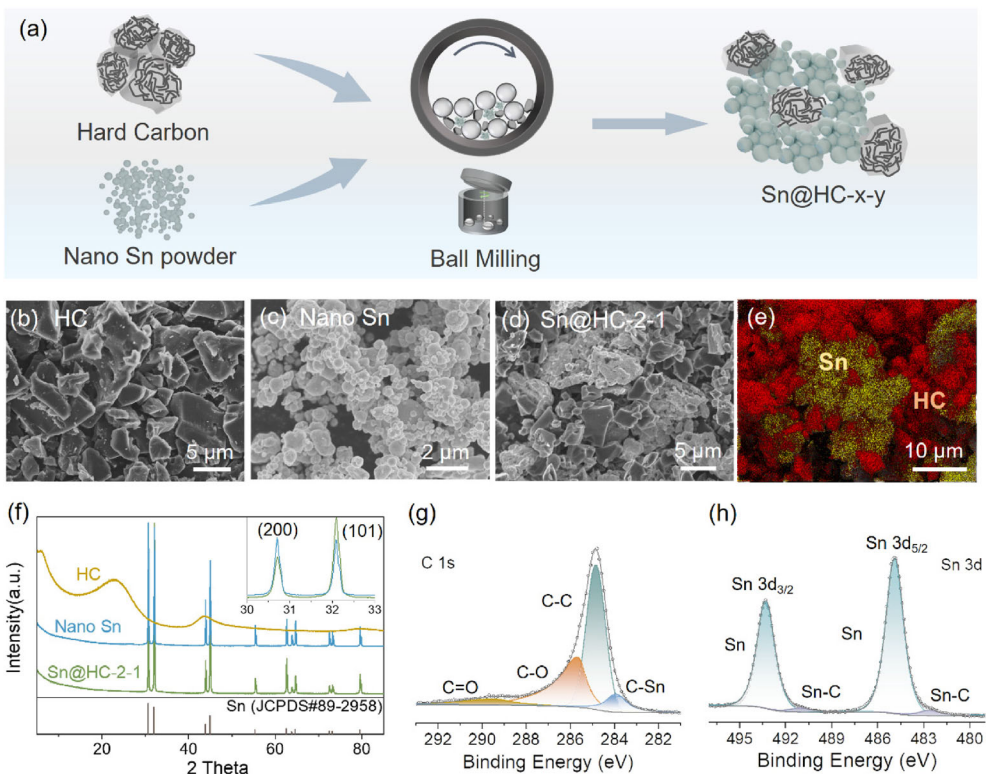


Figure 1. a) Schematic illustration of the synthesis procedure of Sn@HC-x-y composite. b-d) SEM images of HC, nano Sn, and Sn@HC-2-1 materials. e) EDS mapping result of Sn@HC-2-1. f) XRD patterns of different electrodes. The inset shows a local magnification of XRD patterns for nano Sn and Sn@HC-2-1. g,h) C 1s and Sn 3d spectra of Sn@HC-2-1 electrode.

ratio of Sn to HC (see experimental section for details). Commercial HC and nano Sn were used. During ball milling, the soft Sn nanoparticles undergo intense collisions against the rigid HC particles, promoting intimate adhesion and the formation of uniformly distributed Sn-HC heterointerfaces.

Scanning electron microscopy (SEM) images of HC, nano Sn, and Sn@HC-2-1 are presented in Figure 1b-d. Pristine HC appears as irregular particles of $\approx 5 \mu\text{m}$, while nano Sn shows an average particle size of $\approx 100 \text{ nm}$. After ball milling, HC in Sn@HC-2-1 is partly fractured into smaller fragments, which are intimately embedded with Sn nanoparticles to yield a uniform composite morphology (Figure 1d). Energy-dispersive X-ray spectroscopy (EDS) mapping (Figure 1e) confirms abundant, well-distributed Sn-HC interfacial contact. In contrast, reducing the Sn content to form Sn@HC-1-2 leads to a marked diminution of interface contact sites, undermining the formation of a uniformly distributed Sn-HC heterostructure (Figure S1, Supporting Information).

The X-ray diffraction (XRD) peaks for Sn in Sn@HC-2-1 remain basically unchanged (Figure 2f). During ball milling, the dominant diffraction for Sn evolves from (200) to (101) in the inset in Figure 2f, likely associated with the interfacial interactions between Sn and HC.^[26] The amorphous HC signal is obscured by the sharp XRD peaks from Sn.^[27] Figure 1g and h present the surface chemical bonding analysis of Sn@HC-2-1 by X-ray photoelectron spectroscopy (XPS). The C-C (284.8 eV), C-O (285.7 eV), and C=O (289.6 eV) peaks in the C 1s spectra are from

the HC in the composite materials, while the Sn 3d_{3/2} and Sn 3d_{5/2} peaks at 484.9 and 493.3 eV are from the metal Sn.^[28] Notably, both the C 1s (283.9 eV) and Sn 3d (491.1 and 482.7 eV) spectra exhibit new C-Sn peaks, evidencing the mechanochemical formation of Sn-C bonds during ball milling,^[29] and further confirming the establishment of an intact heterointerface structure between Sn and HC.

Cyclic voltammetry (CV) was used to elucidate the impact of the heterointerface on reaction kinetics (Figure 2a-c). Given that the significant overlapping of multiple reduction peaks during discharge complicates the precise electrochemical analysis, we focus on the analysis of the anodic process. At a slow scan rate of 0.2 mV s^{-1} (Figure 2a), the nano Sn electrode exhibits three well-defined anodic peaks at 0.22 V (Sn-O1), 0.57 V (Sn-O2), and 0.71 V (Sn-O3) versus Na⁺/Na, corresponding sequentially to the dealloying transitions $\text{Na}_{15}\text{Sn}_4 \rightarrow \text{Na}_3\text{Sn}_4 \rightarrow \text{NaSn} \rightarrow \text{Sn}$.^[30,31] Interestingly, in Sn@HC-2-1 samples with a heterogeneous interface, a new oxidation peak was observed at $\approx 0.15 \text{ V}$ in addition to the peak corresponding to Sn-O1 at 0.25 V, which could be associated with the interfacial interactions between Sn and HC. This could suggest that the initial phase transition process was essentially regulated by the heterointerfaces in the composite anode. Meanwhile, the oxidation peak potential of Sn-O2 (0.56 V vs. Na⁺/Na) was lower than that of nano Sn (0.57 V vs. Na⁺/Na), suggesting greatly enhanced reaction kinetics. The shoulder peak located at 0.10 V could be due to the oxidation peak of HC in the composite.^[32]

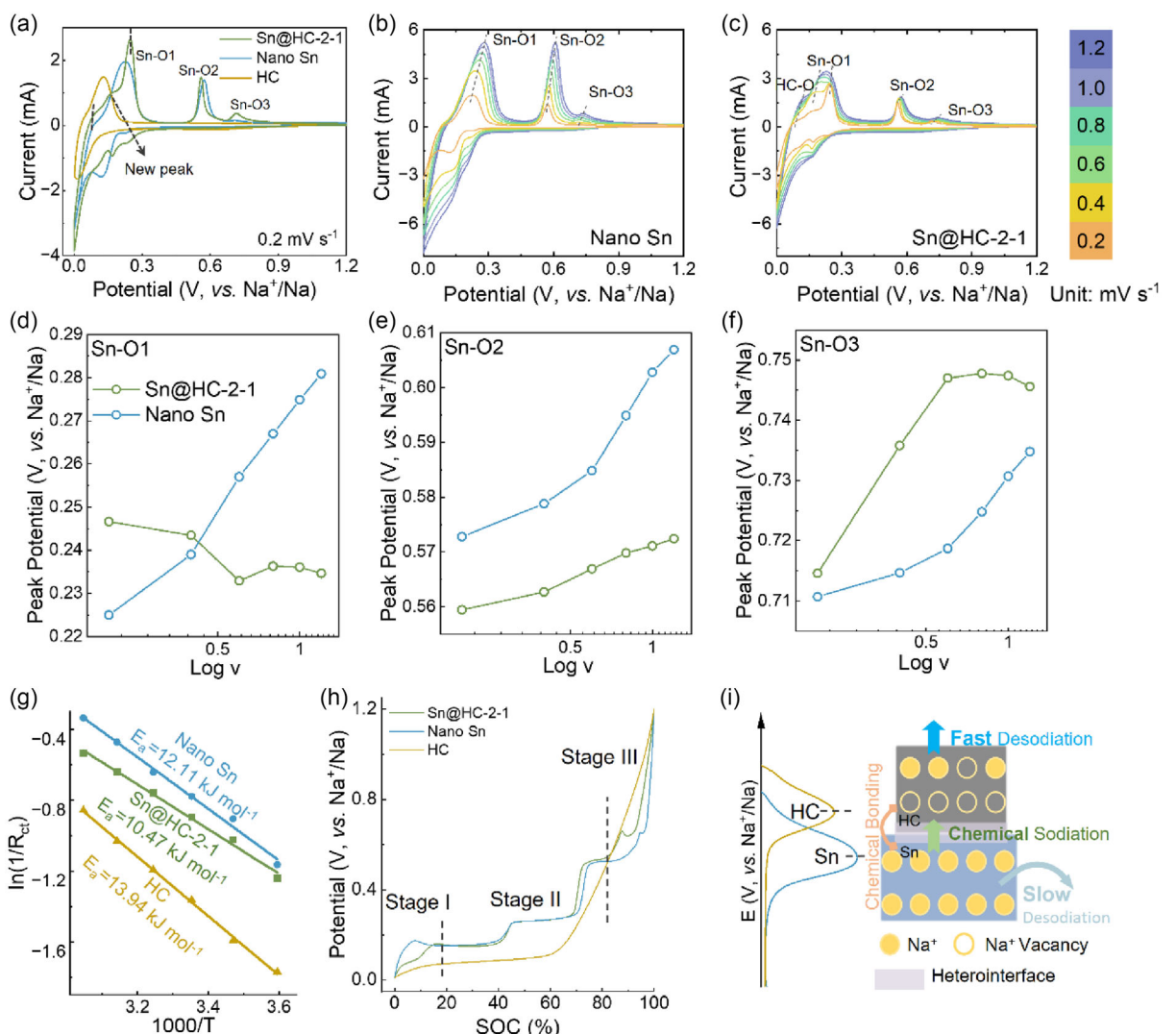


Figure 2. a) CV curves of HC, nano Sn and Sn@HC-2-1 electrodes at 0.2 mV s⁻¹. b,c) CV curves of nano Sn and Sn@HC-2-1 electrodes under variable scan rates. d-f) Plots of peak potentials for Sn-O1, Sn-O2, and Sn-O3 depending on the logarithm of the scan rate. g) Arrhenius curves and comparison of activation energies of HC, nano Sn, and Sn@HC-2-1 electrodes. h) Normalized charge curves for HC, nano Sn, and Sn@HC-2-1 electrodes. i) Illustration of the coupling chemical-electrochemical reactions at the heterointerface between Sn and HC.

Figure 2b–c and S2 present CV profiles for nano Sn, Sn@HC-2-1, and HC at variable scan rates. A systematic analysis of the anodic peak potential as a function of scan rate is shown in Figure 2d–f and Figure S3, Supporting Information. With the increasing scan rate, Sn–O1, Sn–O2, and Sn–O3 in Sn@HC-2-1 all show a significantly suppressed increase in the oxidation potentials compared with the single phase of nano Sn electrode, reflecting the obvious roles of heterointerfaces in enhancing the reaction kinetics of Sn-based anodes. Notably, Sn–O1 peak in Sn@HC-2-1 surprisingly exhibits a slight decrease in overpotential at higher rates. By contrast, the main anodic peaks for single-phase nano Sn display a pronounced rise in overpotentials as the scan rate increases (Figure 3d). Such “abnormal” behavior, on the one hand, verifies greatly enhanced reaction kinetics in the composite anode, and on the other hand, suggests an additional reaction pathway for the alloying/dealloying reactions with fast charge transfer kinetics.

As depicted in Figure S4, Supporting Information, the Na-ion diffusion coefficients of Sn@HC-2-1 range from 10^{-15} – 10^{-10} cm² s⁻¹, far surpassing that of nano Sn (10^{-18} to 10^{-12} cm² s⁻¹). The introduction of synergistic coupling heterointerface with fast kinetics can simultaneously enhance the reaction kinetics and improve the electrochemical performance.

Variable temperature electrochemical impedance spectroscopy (EIS) further demonstrates significantly lower apparent activation energy for the Sn@HC-2-1 electrode (Figure 2g). Nyquist plots of HC, nano Sn, and Sn@HC-2-1 electrodes at various temperatures (Figure S5, Supporting Information) were fitted using the equivalent circuit in Figure S6, Supporting Information, via nonlinear least squares, determining R_s, R_{SEH}, R_{ct}, and R_{diff}. Sn@HC-2-1 exhibited lower R_{ct} values than HC and values comparable to nano Sn, indicating retention of the efficient charge transfer characteristics of the nanomaterial. Fitting R_{ct} data to the Arrhenius equation yielded apparent activation energies.

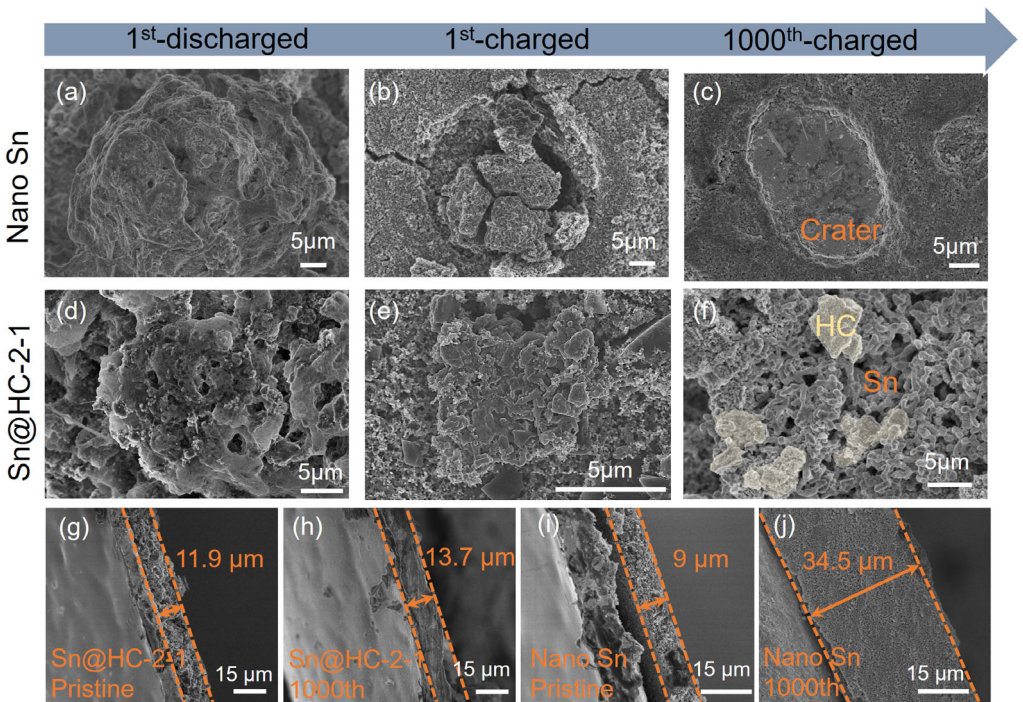


Figure 3. SEM images of Sn-based electrodes at fully discharged state, after 1 cycle, and after 1000 cycles for nano Sn a–c) and Sn@HC-2-1 d–f) electrodes. SEM images of the pristine and cycled electrode after 1000 cycles for Sn@HC-2-1 g,h) and nano Sn i,j) electrodes.

The Sn@HC-2-1 electrode exhibited the lowest E_a ($10.47 \text{ kJ mol}^{-1}$), corresponding to reductions of $\approx 13\%$ and 25% compared to the monocomponent nano Sn ($12.11 \text{ kJ mol}^{-1}$) and HC ($13.94 \text{ kJ mol}^{-1}$) electrodes, respectively (Figure 2g).

The charge curves of different anodes were normalized to further elucidate the modulation functions of heterointerfaces in Figure 2h–i. The charging curves can be roughly divided into three stages. In stage I, the dealloying of single-phase nano Sn exhibits a pronounced overpotential. By contrast, such substantial overpotential in the Sn@HC-2-1 electrode is not observed. The HC phase in the Sn@HC-2-1 undergoes prior Na extraction because of faster desodiation kinetics and lower desodiation potential of HC.^[9,33,34] This preferential Na extraction from HC immediately establishes a localized electrochemical-potential difference between Sn and desodiated HC, which in turn drives the chemical sodiation reaction of $\text{Na}_{15}\text{Sn}_4$ towards the relatively Na-deficient HC phase. This interfacial charge transfer dramatically lowers the energy barrier for $\text{Na}_{15}\text{Sn}_4$ dealloying. Besides, in the discharge process, the existing charge transfer at the heterointerface between Sn and HC is also beneficial to the reaction kinetics.

During the main stage of Na extraction (stage II), the HC remains constantly lower desodiation potential than the Sn phase. The electrochemical-potential difference at the heterointerfaces between Sn and HC provides an additional driving force for the dealloying reaction of Sn. This explains the CV results in Figure 2b–d. Simultaneously, the charge transfer between the heterointerface adjusts automatically to avoid the severe volumetric expansion of the alloying product of $\text{Na}_{15}\text{Sn}_4$ (as discussed below).^[35,36] During stage III, desodiated HC continues to propel

the final dealloying steps of Sn which is consistent with the reduced overpotential for Sn-O3 peaks in Figure 3f. It is noted that the promotion impact of the heterointerfaces between Sn and HC is sensitively related to the mass ratio of Sn and HC (Figure S7, Supporting Information). A lower proportion of HC in the Sn/HC composite cannot establish a sufficient local electrochemical-potential difference network to promote the reaction kinetics, while a higher proportion of HC will significantly reduce the specific capacity advantage of the alloy anodes.

Severe volume expansion and particle pulverization during cycling represent another critical challenge for alloy-based anodes in practical use.^[37,38] SEM was performed to morphology changes of Sn-based anodes after cycling. As shown in Figure 3a–c, the single-phase nano Sn electrode exhibits pronounced particle agglomeration and significant swelling after the first discharge, with particle size reaching $48 \mu\text{m}$ (685% expansion). Dramatic particle contraction produces craters and cracks of $\approx 34 \mu\text{m}$ on the electrode surface after just one cycle. After 1000 cycles, the nano Sn electrode is covered with numerous residual craters from detached active particles. The degraded electrode structural stability may severely undermine the cycling stability of the alloy anode.

By contrast, the Sn@HC-2-1 active material exhibits a particle size of $\approx 19 \mu\text{m}$ at the fully sodiated state during the first cycle, indicating a volume expansion of $\approx 250\%$. The Sn@HC-2-1 electrode exhibits substantially less particle expansion after discharge, with no evidence of cracking or fragmentation. Sn particles remain in intimate contact with surrounding HC and display particle sizes comparable to those of the pristine composite after charge (Figure 3d–e). Remarkably, even after 1000 cycles, the

Sn@HC-2-1 electrode still maintains basically close contact between Sn and HC. Figure 3f highlights densely adhered HC fragments both around and within the coral-like Sn network (yellow regions). The HC phase in the Sn@HC-2-1 composite offers rapid desodiation kinetics and negligible volume change (Figure S8, Supporting Information). The coupling chemical-electrochemical reactions at the heterointerface sustain a quasi-synchronous Na-storage potential between HC and Sn. Therefore, the appropriate heterointerfaces play a flexible role in automatically regulating the local electrochemical potential inside the electrode. Swift interfacial charge transfer provides an interesting and useful strategy to tackle the complex issues of alloy anodes with large volume expansion and slow kinetics.

Figure 3g–h display the cross-sectional SEM images of the pristine and Sn@HC-2-1 electrodes after 1000 full cycles. Remarkably, the electrode thickness increases only from initial 11.9 to 13.7 μm (a mere 15% expansion), still showing a dense and well-integrated electrode. The stable Sn@HC-2-1 electrode after long cycles verifies the unique function of introducing appropriate heterointerfaces into alloy anodes to buffer the volume change via interfacial charge transfer. In contrast, the nano Sn electrode swells from 9.0 to 34.5 μm after 1000 cycles, accompanied by a 280% expansion (Figure 3i–j). Furthermore, the porosity of the nano Sn electrode increases significantly. The loose electrode reduces the adhesion of the active material and causes extensive delamination from the current collector and the crater formation as observed in Figure 3c.^[39] Interestingly, even

the Sn@HC-1-2 electrode with even lower Sn content exhibits a higher volume expansion than the Sn@HC-2-1 electrode (Figure S9, Supporting Information). These results further indicate that the appropriate ratio of HC and Sn in the alloy composite plays a key role in the rational use of the electrochemical potential difference between the two phases. By facilitated interfacial charge transfer, the heterointerfaces suppress excessive formation of $\text{Na}_{15}\text{Sn}_4$ alloy phase with huge volume expansion, thereby preserving excellent electrode structural stability.^[40]

Stable electrode-electrolyte interphase is essential for achieving prolonged cycle life of alloy-type anodes.^[41] High-resolution transmission electron microscopy (HRTEM) was used to examine the SEI morphology of cycled Sn@HC-2-1 and nano Sn electrodes (Figure 4a–d). After 1000 cycles, the Sn@HC-2-1 electrode retains a thin and uniform SEI layer of ≈ 2 nm thick, suggesting excellent interfacial stability of the composite electrode. In sharp contrast, the nano Sn electrode shows a thick and rough SEI, with a maximum local thickness approaching 17 nm.

XPS depth profiles indicate an organic-inorganic mixed SEI on the Sn@HC-2-1 electrode after prolonged cycling, which includes organic species (C—OR, C=O, C—F) and inorganic constituents (NaF, Na_2O) in Figure 4e–g. Notably, the inner SEI layer is rich in inorganic salts such as NaF and Na_2PO_4 , which facilitates excellent ionic conductivity and mechanical robustness of SEI layer. The relatively minor organic fraction, derived mainly from the decomposition and polymerization of the DEGDME solvent, weaves a flexible organic network throughout the SEI to

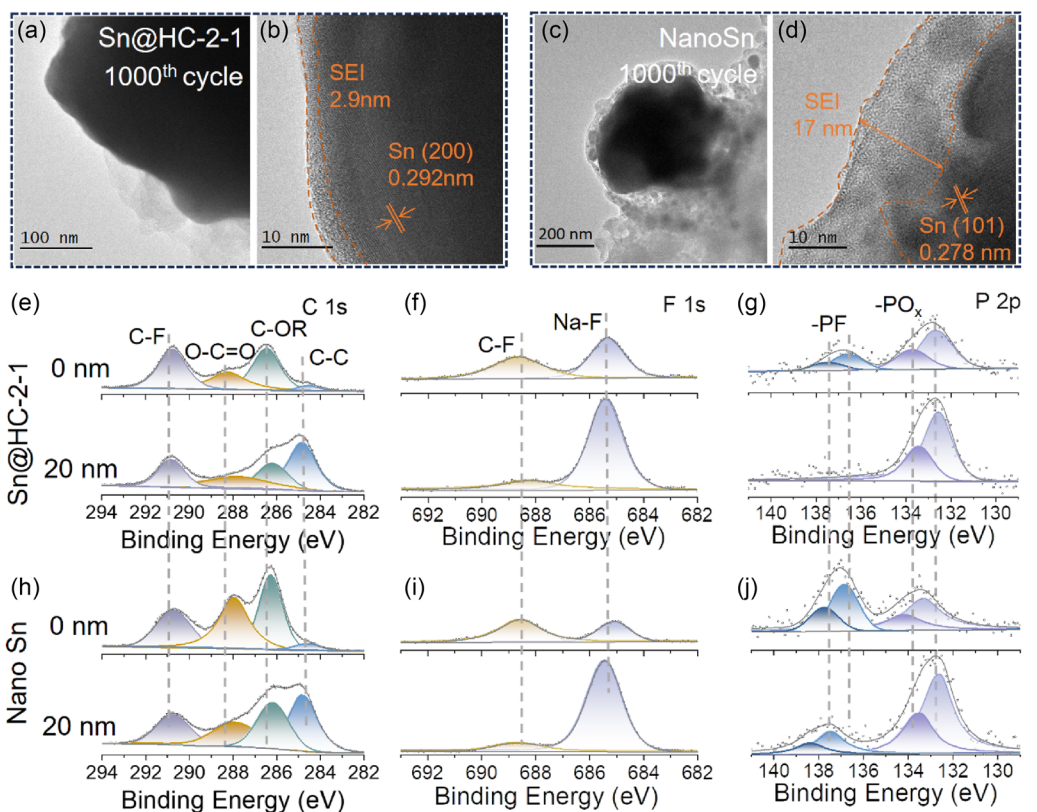


Figure 4. HRTEM images of a,b) Sn@HC-2-1 and c,d) nano Sn anode after 1000th cycle. XPS depth profiles of C 1s, F 1s, and P 2p of Sn@HC-2-1 anodes e–g) and nano Sn anode h–j) nano Sn.

accommodate the volume changes of Sn-based anode.^[42–44] These findings are consistent with the dense, uniform SEI morphology of the Sn@HC-2-1 electrode in Figure 4b. Nano Sn electrode exhibits a similar SEI composition as derived from the same electrolyte, but the contents of organic species (e.g., C—OR, C=O) and PF_x fragments from NaPF₆ decomposition are significantly higher (Figure 4h–j). This can be attributed to repeated SEI fracture and reformation of the nano Sn electrode during cycling, failing to prevent continuous electrolyte decomposition.^[45]

The electrochemical performance of the Sn@HC-2-1 electrode is thoroughly investigated in Figure 5. With one third by mass of HC, the theoretical specific capacity of Sn@HC-2-1 is 664 mAh g⁻¹. As shown in Figure 5a, Sn@HC-2-1 delivers an initial reversible capacity of 613 mAh g⁻¹ and an initial Coulombic efficiency of 83.1% at 0.08 A g⁻¹, markedly outperforming both HC (72.3%) and the single-phase of nano Sn (80.1%). In Sn@HC-2-1 composite, HC only contributes ≈95 mAh g⁻¹ at 0.08 A g⁻¹ (285 mAh g⁻¹ for pure HC electrode). The Sn@HC-2-1 presents the capacity of 540, 533, 527, 507, 449, and 186 mAh g⁻¹ at current densities of 0.17, 0.42, 0.84, 1.7, 4.2, and 8.4 A g⁻¹ (Figure 5b, S10, Supporting

Information), which far exceeds those of conventional HC anodes. Furthermore, even at elevated mass loadings, the Sn@HC-2-1 maintains excellent rate performance (Figure S11, Supporting Information). Figure 5c shows the charge-discharge profiles of Sn@HC-2-1 at 0.08–4.2 A g⁻¹. The nearly overlapped voltage curves of Sn@HC-2-1 at 4.2 A g⁻¹ indicate minimal polarization and fast reaction kinetics. This outstanding rate performance could stem from the optimized heterointerface in the composite alloy anode.

In addition, the Sn@HC-2-1 composite anode exhibits outstanding long-term cycling stability (Figure 5d–e). At 1.7 A g⁻¹, the electrode delivers an initial reversible capacity of 497 mAh g⁻¹ and sustains stable operation for up to 12 000 cycles. Between 400 and 12 000 cycles, the capacity decays only from 374 to 270 mAh g⁻¹, corresponding to a 72% retention. The HC anode, which also demonstrates stable cycling at 1.7 A g⁻¹, suffers from a low initial capacity of only 190 mAh g⁻¹ (38% of the capacity of Sn@HC-2-1). Sn@HC-2-1 anode maintains a reversible capacity of 443 mAh g⁻¹ at higher current of 4.2 A g⁻¹, which still achieves an impressive 83% capacity retention from cycle 200 to 12 000 (Figure 5e). By contrast, although the monophase nano Sn

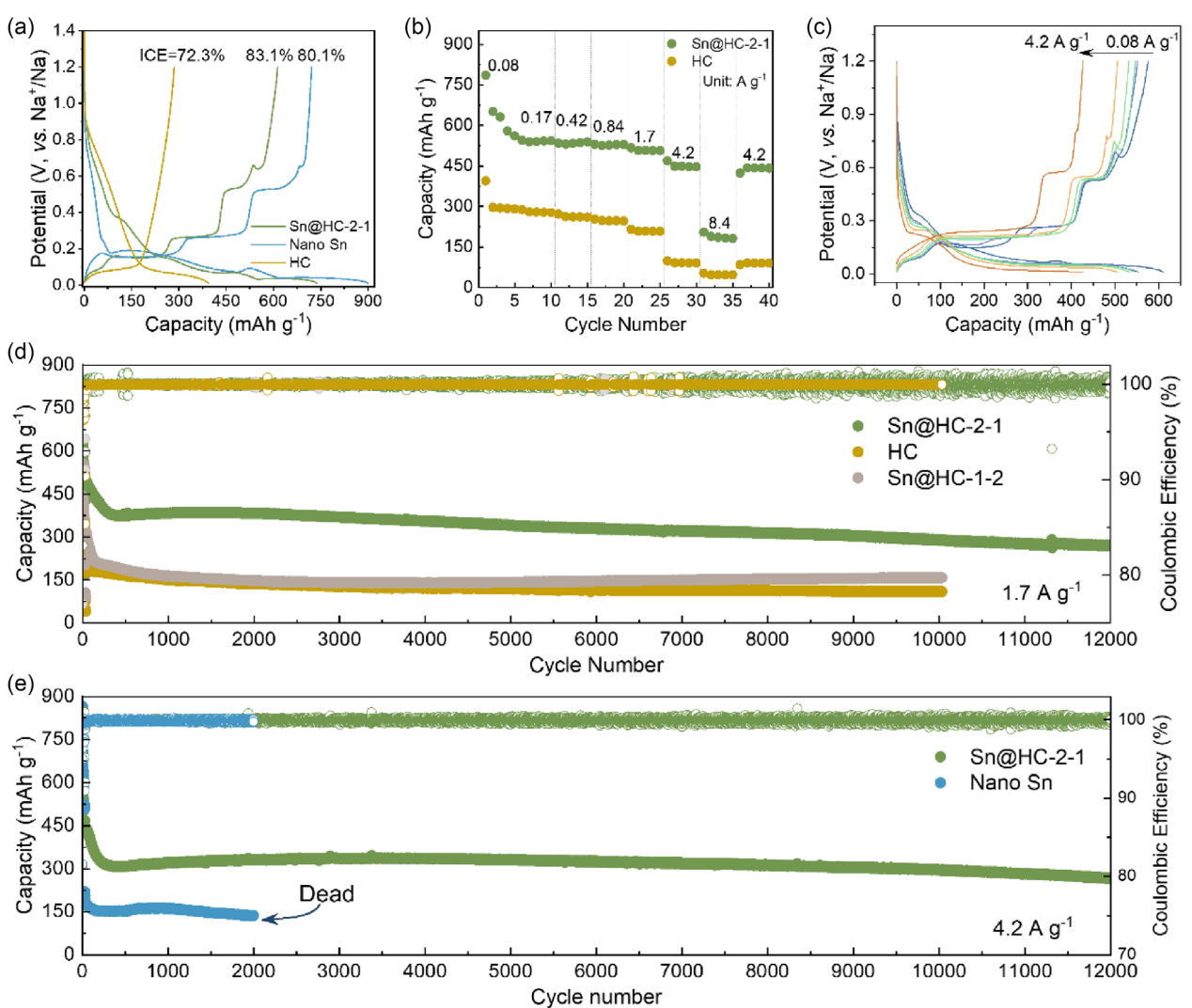


Figure 5. a,b) Galvanostatic discharge–charge curves and rate performance of Sn@HC-2-1, nano Sn, and HC electrodes. c) Galvanostatic discharge–charge curves of Sn@HC-2-1 electrode at different C rates. d,e) Cycling performance of Sn@HC-2-1 electrode at 1.7 and 4.2 A g⁻¹.

electrode shows a slightly higher capacity in low current density, it fails after just 1964 cycles at 4.2 A g^{-1} , likely due to internal soft shorting caused by severe volumetric changes of Sn.^[46] Moreover, the NFM||Sn@HC-2-1 full cell delivers an initial reversible capacity of 548 mAh g^{-1} and achieves a 67% capacity retention after 300 cycles (Figure S12, Supporting Information). The excellent rate and cycling stability of Sn@HC-2-1 demonstrate that introducing an appropriate heterointerface into alloy anodes is an effective strategy for addressing the complex challenges in alloy anodes.

3. Conclusion

This study provides an effective strategy to address the critical challenges of Sn-based alloy anodes in NIBs, i.e., severe volume expansion, sluggish kinetics, and limited cycle life. A simple ball-milling approach is used to establish well-matched heterointerfaces between the Sn and HC phases. This unique heterointerface facilitates efficient charge transfer driven by local electrochemical-potential differences, enabling dynamic regulation of the alloying reaction pathway and effective mitigation of volume strain. The chemically-electrochemically coupling heterointerface not only significantly enhances the reaction kinetics and reversibility but also suppresses the severe volume change and enables stable electrode-electrolyte interphases. This work provides valuable insights into the role of multiscale interface design in alleviating the volume effects of alloy-type anodes and offers practical guidance for the use of alloy anodes.

Acknowledgements

This work was supported by the Jianbing Science and Technology Key Project of Zhejiang Province (2025C01156), the Zhejiang Provincial Natural Science Foundation of China under grant no. LR23B030003, the National Natural Science Foundation of China (grant nos. U21A2075 and 22179117), and the National Key R&D Program of China, grant no. 2022YFB2404700.

Conflict of Interest

The authors declare no conflict of interest.

Data Availability Statement

The data that support the findings of this study are available from the corresponding author upon reasonable request.

Keywords: electrochemical-potential • heterointerface • Na-ion batteries • Sn-based anodes

- [1] W. Zhao, H. Dong, Z. Xing, L. Zhou, S. Chen, H.-K. Liu, S.-X. Dou, Z. Zhao, H. Xia, S. Chou, M. Chen, *Adv. Energy Mater.* **2024**, *14*, 2402720.
- [2] P. X. Bai, X. P. Han, Y. W. He, P. X. Xiong, Y. F. Zhao, J. Sun, Y. H. Xu, *Energy Storage Materials* **2020**, *25*, 324.

- [3] C. Shi, D. Muhtar, X. Lu, F. Liu, X. Lu, Z. Sun, Z. Guo, *Adv. Energy Mater.* **2025**, *15*, 2500448.
- [4] Z. Chen, T. Tao, C. Shi, X. Shi, L. Shao, J. Xu, Z. Sun, *Carbon Neutralization* **2025**, *4*, e70010.
- [5] C. Zhang, B. Chen, Q. Chen, Y. Liu, X. Kong, L. Suo, J. Lu, H. Pan, *Adv. Mater.* **2024**, *36*, 2405913.
- [6] S. Wu, H. Peng, J. Xu, L. Huang, Y. Liu, X. Xu, Y. Wu, Z. Sun, *Carbon* **2024**, *218*, 118756.
- [7] X. Nie, Z. Chen, B. Deng, L. Shao, J. Xu, X. Shi, Z. Sun, *Adv. Energy Mater.* **2025**, *15*, 2500069.
- [8] J. Xiao, Q. Li, Y. Bi, M. Cai, B. Dunn, T. Glossmann, J. Liu, T. Osaka, R. Sugiura, B. Wu, J. Yang, J.-G. Zhang, M. S. Whittingham, *Nat. Energy* **2020**, *5*, 561.
- [9] H. Zhou, Y. Song, B. Zhang, H. Sun, I. A. Khurshid, Y. Kong, L. Chen, L. Cui, D. Zhang, W. Wang, L. Yang, X. Du, *Energy Storage Mater.* **2024**, *71*, 103645.
- [10] X. Lu, J. Zhou, L. Huang, H. Peng, J. Xu, G. Liu, C. Shi, Z. Sun, *Adv. Energy Mater.* **2024**, *14*, 2303081.
- [11] K. Song, C. Liu, L. Mi, S. Chou, W. Chen, C. Shen, *Small* **2021**, *17*, 1903194.
- [12] H. Li, L. Peng, Y. Zhu, D. Chen, X. Zhang, G. Yu, *Energy Environ. Sci.* **2016**, *9*, 3399.
- [13] W. Luo, F. Shen, C. Bommier, H. Zhu, X. Ji, L. Hu, *Acc. Chem. Res.* **2016**, *49*, 231.
- [14] J. W. Wang, X. H. Liu, S. X. Mao, J. Y. Huang, *Nano Lett.* **2012**, *12*, 5897.
- [15] E. Olsson, J. Yu, H. Zhang, H. M. Cheng, Q. Cai, *Adv. Energy Mater.* **2022**, *12*, 2200662.
- [16] J. Luo, M. Xue, K. Song, Z. Xie, W. Meng, W. Li, X. Li, X. Guo, J. Ge, L. Wen, W. Chen, *Science China Chemistry* **2025**, *68*, 2059.
- [17] R. Mo, X. Tan, F. Li, R. Tao, J. Xu, D. Kong, Z. Wang, B. Xu, X. Wang, C. Wang, J. Li, Y. Peng, Y. Lu, *Nat. Commun.* **2020**, *11*, 1374.
- [18] X. Wu, X. Lan, R. Hu, Y. Yao, Y. Yu, M. Zhu, *Adv. Mater.* **2022**, *34*, e2106895.
- [19] C. Zhang, B. Chen, Q. Chen, C. Tian, M. Zhou, X. Zhao, Z. Li, L. Fan, X. Kong, H. Pan, *ACS Energy Lett.* **2024**, *9*, 4691.
- [20] T. Palanisvam, M. Goktas, B. Anothumakool, Y. N. Sun, R. Schmuck, L. Zhao, B. H. Han, M. Winter, P. Adelhelm, *Adv. Funct. Mater.* **2019**, *29*, 1900790.
- [21] Y. Liu, N. Zhang, L. Jiao, J. Chen, *Adv. Mater.* **2015**, *27*, 6702.
- [22] Z. Xu, J. Ye, Y. Pan, K. Liu, X. Liu, J. Shui, *Energy Technology* **2022**, *10*, 2101024.
- [23] Y. Liu, N. Zhang, L. Jiao, Z. Tao, J. Chen, *Adv. Funct. Mater.* **2014**, *25*, 214.
- [24] M. Lao, Y. Zhang, W. Luo, Q. Yan, W. Sun, S. X. Dou, *Adv. Mater.* **2017**, *29*, 1700662.
- [25] Y. Wan, B. Huang, W. Liu, D. Chao, Y. Wang, W. Li, *Adv. Mater.* **2024**, *36*, e2404574.
- [26] L. Baggetto, P. Ganesh, R. P. Meissner, R. R. Unocic, J.-C. Jumas, C. A. Bridges, G. M. Veith, *J. Power Sources* **2013**, *234*, 48.
- [27] Q. Li, W. Zhang, J. Peng, W. Zhang, Z. Liang, J. Wu, J. Feng, H. Li, S. Huang, *ACS Nano* **2021**, *15*, 15104.
- [28] M. Ma, H. Cai, C. Xu, R. Huang, S. Wang, H. Pan, Y.-S. Hu, *Adv. Funct. Mater.* **2021**, *31*, 2100278.
- [29] X.-T. Chen, K.-X. Wang, Y.-B. Zhai, H.-J. Zhang, X.-Y. Wu, X. Wei, J.-S. Chen, *Dalton transactions* **2014**, *43*, 3137.
- [30] J. Yang, X. Guo, H. Gao, T. Wang, Z. Liu, Q. Yang, H. Yao, J. Li, C. Wang, G. Wang, *Adv. Energy Mater.* **2023**, *13*, 2300351.
- [31] L. D. Ellis, T. D. Hatchard, M. N. Obrovac, *J. Electrochem. Soc.* **2012**, *159*, A1801.
- [32] X. Lu, J. Zhou, X. Li, H. Peng, C. Shi, F. Liu, L. Huang, Z. Sun, *ACS Appl. Mater. Interfaces* **2025**, *17*, 29708.
- [33] J. Wang, H. Yin, Z. Wang, J. Gao, Q. Jiang, Y. Xu, Z. Chen, *Asia-Pac. J. Chem. Eng.* **2022**, *17*, e2768.
- [34] S. Zhao, Z. Guo, J. Yang, C. Wang, B. Sun, G. Wang, *Small* **2021**, *17*, e2007431.
- [35] S. Guo, Z. Sun, Y. Liu, X. Guo, H. Feng, S. Luo, C. Wei, Y. Zheng, X. Zhang, K. Kim, H. Liu, P. K. Chu, B. Gao, Q. Zhang, K. Huo, *Adv. Energy Mater.* **2024**, *14*, 23003876.
- [36] C. Kim, K.-Y. Lee, I. Kim, J. Park, G. Cho, K.-W. Kim, J.-H. Ahn, H.-J. Ahn, *J. Power Sources* **2016**, *317*, 153.
- [37] C. Wu, G. Zhu, Q. Wang, M. Wu, H. Zhang, *Energy Storage Mater.* **2021**, *43*, 430.
- [38] J. Wang, C. Eng, Y. C. Chen-Wiegart, J. Wang, *Nat. Commun.* **2015**, *6*, 7496.
- [39] S. Dong, L. Wang, X. Huang, J. Liang, X. He, *Adv. Funct. Mater.* **2024**, *34*, 2404192.

- [40] H. Yang, L. Y. Yang, A. Abiliz, S. Y. Wang, F. J. Zhao, M. Zhang, J. Li, H. B. Li, *Ionics* **2021**, *27*, 1429.
- [41] Y. Tian, Y. An, B. Zhang, *Adv. Energy Mater.* **2023**, *13*, 2300123.
- [42] Y. Wang, P. Bai, B. Li, C. Zhao, Z. Chen, M. Li, H. Su, J. Yang, Y. Xu, *Adv. Energy Mater.* **2021**, *11*, 2101972.
- [43] J. Zhang, D.-W. Wang, W. Lv, S. Zhang, Q. Liang, D. Zheng, F. Kang, Q.-H. Yang, *Energy Environ. Sci.* **2017**, *10*, 370.
- [44] J. Ge, C. Ma, Y. Zhang, P. Ma, J. Zhang, Z. Xie, L. Wen, G. Tang, Q. Wang, W. Li, X. Guo, Y. Guo, E. Zhang, Y. Zhang, L. Zhao, W. Chen, *Adv. Mater.* **2024**, 2413253.
- [45] J. Luo, K. Yang, J. Gai, X. Zhang, C. Peng, C. Qin, Y. Ding, Y. Yuan, Z. Xie, P. Yan, Y. Cao, J. Lu, W. Chen, *Angew. Chem. Int. Ed.* **2025**, *64*, e202419490.
- [46] Y. Wang, R. Ou, J. Yang, Y. Xin, P. Singh, F. Wu, Y. Qian, H. Gao, *Journal of Energy Chemistry* **2024**, *95*, 407.

Manuscript received: May 29, 2025

Revised manuscript received: July 10, 2025

Version of record online:
